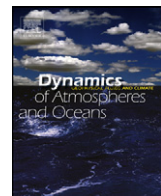




Contents lists available at ScienceDirect

## Dynamics of Atmospheres and Oceans

journal homepage: [www.elsevier.com/locate/dynatmoce](http://www.elsevier.com/locate/dynatmoce)



# Changes in upwelling and its water sources in the California Current System driven by different wind forcing

Hajoon Song<sup>a,\*</sup>, Arthur J. Miller<sup>a</sup>, Bruce D. Cornuelle<sup>a</sup>, Emanuele Di Lorenzo<sup>b</sup>

<sup>a</sup> Scripps Institution of Oceanography, University of California, San Diego, La Jolla 92093-0224, USA

<sup>b</sup> School of Earth and Atmospheric Sciences, Georgia Institute of Technology, Atlanta, USA

## ARTICLE INFO

Available online 2 April 2011

### Keywords:

California Current System  
Upwelling  
Wind stress curl  
Upwelling source waters  
Adjoint model

## ABSTRACT

In the California Current System (CCS), upwelling is one of the most important features that enrich the coastal ecosystem. It is highly dependent on both wind stress and wind stress curl, because they contribute to the upwelling system through Ekman transport away from the coast and Ekman pumping as a result of the surface divergence, respectively. Various wind stress products are known to contain sharply different patterns of wind stress, and well-resolved wind forcing products have been shown to drive stronger upwelling due to their better-resolved wind stress curl in previous studies. However, sensitivities of upwelling to changes in wind stress patterns, and each of their control to the source waters and paths of the upwelling cells, are not yet well known for the CCS. Here we study these effects using the Regional Ocean Modeling System (ROMS) and its adjoint model under idealized wind stress forcing patterns representing three widely-used products in addition to a constant wind stress field (no curl): the NCEP/NCAR Reanalysis, the QuikSCAT satellite observations, and the Regional Spectral Model (RSM) downscaling.

Changes in currents and isopycnal patterns during the upwelling season are first studied in ROMS under the four different wind stress fields. The model simulations show that the locations of the core of the equatorward flow and the gradient of the cross-shore isopycnals are controlled by the wind stress curl field. The core of the equatorward flow is found under negative wind stress curl, and a deeper upwelling cell is found as the gradient from positive and negative wind stress curl increases. Source waters for the upwelling

\* Corresponding author. Tel.: +1 8588224061.  
E-mail address: [j0song@ucsd.edu](mailto:j0song@ucsd.edu) (H. Song).

in each of the four wind stress patterns are investigated using the ROMS adjoint model. The simulations follow a passive tracer backward in time and track the source waters for upwelling in two key areas of interest: inshore and offshore of the Point Sur region of California. The upwelling source waters depend strongly on the depth of the upwelling cell and the alongshore current location. We further relate these results to recent studies of the observed trends in upwelling favorable winds and consequent wind stress curl changes in the CCS.

© 2011 Elsevier B.V. All rights reserved.

## 1. Introduction

One of the distinguishing characteristics of the California Current System (CCS) is its wind-driven upwelling, which provides nutrient-rich water to the euphotic zone, supporting a productive ecosystem. Two mechanisms are primarily responsible for this wind driven upwelling. The first is Ekman transport. As the wind blows equatorward alongshore with timescales greater than the Coriolis frequency, it pushes the surface water offshore. As a result, cool, nutrient-rich subsurface water is lifted up to the surface along the continental slope. It is often referred as coastal upwelling because it occurs only in narrow regions near the coast. The second is Ekman pumping. With cyclonic (positive) wind stress curl, divergence of the surface water brings the subsurface water to the surface in order to conserve mass. This upwelling usually happens in broader regions where the wind stress curl is positive, and offshore upwelling is associated with this mechanism (Chelton, 1982; McCreary et al., 1987).

Developing a better understanding of the intricacies of these mechanisms has been of great interest to many scientists. Related research includes not only the classic efforts to understand the upwelling physical processes (Sverdrup et al., 1942; Smith, 1968), but also many recent observational, seagoing and modeling studies. In particular, the role of the wind stress curl in eastern-boundary upwelling processes has drawn increased attention.

Using the 9 km resolution wind reanalysis data from the Coupled Ocean/Atmosphere Mesoscale Prediction System (COAMPS), Pickett and Paduan (2003) estimated the vertical transport by Ekman pumping and Ekman transport at four different locations along the California coast. They showed that both Ekman pumping and Ekman transport are important for upwelling in the CCS. Chelton (1982) argued that the high concentrations of chlorophyll near the coast can be linked to coastal upwelling, while the maximum of zooplankton biomass at offshore locations during spring-summer is indirectly related to the offshore upwelling by Ekman pumping. Rykaczewski and Checkley (2008) found an increasing trend of curl-driven upwelling in their analysis, while the coastal upwelling remained nearly constant. Also, they noted a positive correlation between wind stress curl and biological water properties such as chlorophyll-a concentration, nutricline depth and isopycnal shoaling as well as sardine productivity over the last few decades in the CCS.

Wind stress curl is computed from the wind stress field, so the accuracy of the curl-driven upwelling estimate is dependent on accuracy of the wind stress field. Winant and Dorman (1997) analyzed seasonal wind stress and wind stress curl over the Southern California Bight based on data from the California Cooperative Oceanic Fisheries Investigations (CalCOFI) program and from moored buoys. Using a  $0.2^\circ$  grid, their estimated maximum wind stress curl during the spring is  $3 \times 10^{-6} \text{ N m}^{-3}$  which is almost three times the estimate by Nelson (1977) in which a  $1^\circ$  grid was used. So they suggested that wind forcing resolution should include scales of the order of tens of kilometers in order for models to predict ocean states successfully. Capet et al. (2004) tested an ocean model (Regional Ocean Modeling System (ROMS)) response to the alongshore wind stress structure. The model had a secondary upwelling core roughly 15–30 km offshore, which may indicate open-ocean Ekman pumping associated with another 9 km resolution COAMPS wind stress. This product has a big drop-off in stress at the coast, resulting in strong changes in alongshore velocity. On the other hand, no secondary upwelling core was observed in the model with NASA's Quick Scatterometer (QuikSCAT) forcing, whose wind stress values within ~50 km of the coast must be filled with an objective analysis, resulting in a weak

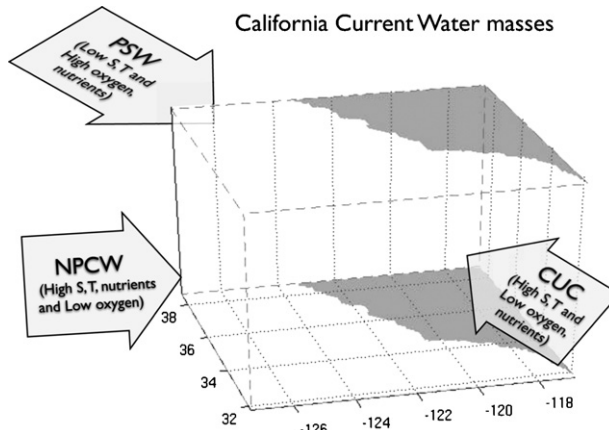


**Fig. 1.** Three water masses that contribute the California Current System, and their characteristics. Pacific Subarctic water (PSW) that has low salinity, temperature and high oxygen, nutrients comes from the north, North Pacific Central water (NPCW) that has high salinity, temperature, nutrients and low oxygen comes from the west and California undercurrent (CUC) that has high salinity, temperature and low oxygen, nutrients comes from the south.

drop-off of wind stress near the coast. The wind stress and the wind stress curl can significantly be affected by the orography. Pickett and Paduan (2003) showed the major coastal promontories along the California coast can intensify the wind stress and curl in their COAMPS with 9 km resolution. Doyle et al. (2009) showed that their 3 km resolution COAMPS produced the strongest orographic influences on the wind stress curl, compared to the 9 km and 27 km meshes.

Although it was confirmed that curl-driven upwelling could vary depending on the wind stress resolution, the details of how it changes the upwelling source waters and the mechanisms that are responsible for bringing the upwelled water from depth are still unclear. This lack of understanding is partially because strong mesoscale eddies and frontal features, irregular coastlines, coastal orographic structures, and strongly variable winds combine to produce an intricate circulation that can be best understood by analyzing observations and model simulations together. The two upwelling mechanisms complicate the attribution of upwelling water sources. The coastal upwelling is associated with the equatorward flow of cold water (Di Lorenzo, 2003), while the Ekman pumping drives the poleward flow of warm water (McCreary et al., 1987). Combined with the upwelling, it is not simple to quantify the contribution of water sources to the upwelling zone with a conventional forward model.

Identifying the upwelling water sources is important because the characteristics of upwelling water depend on where the water originates. Marchesiello et al. (2003) identified the characteristics of the large-scale currents that comprise the California current system. As shown in Fig. 1, low salinity, low temperature, high oxygen and nutrient-rich Pacific subarctic water arrives from the north, high salinity, high temperature, nutrient-poor, and low oxygen North Pacific Central water enters from the west, and high salinity, high-temperature, low oxygen, nutrient-rich California undercurrent comes from the south. Thus, the upwelled water could have the characteristics of any of these three sources, or a combination of them.

Finding the upwelled water source is particularly important to understand several biogeochemical processes that have drawn attention in recent years. Historically a thin oxygen minimum zone has been found in water deeper than  $-400\text{ m}$  in the CCS (Helly and Levin, 2004). In recent years, however, the oxygen minimum zone has been shallower and hypoxic, in which the dissolved oxygen (DO) is less than  $1.4\text{ ml l}^{-1}$ , has been observed along the west coast of North America (Bograd et al., 2008). Even anoxia has been reported on the inner shelf off the Oregon coast (Chan et al., 2008). Hypoxic water is deadly to marine life, and the reasons for these phenomena are under investigation, focused on changes in upwelling water source, wind forcing, as well as other factors (Checkley and Barth, 2009).

Adjoint methods have been used to identify source waters in various parts of the world ocean (Fukumori et al., 2004; Chhak and Di Lorenzo, 2007). In particular, Chhak and Di Lorenzo (2007) used

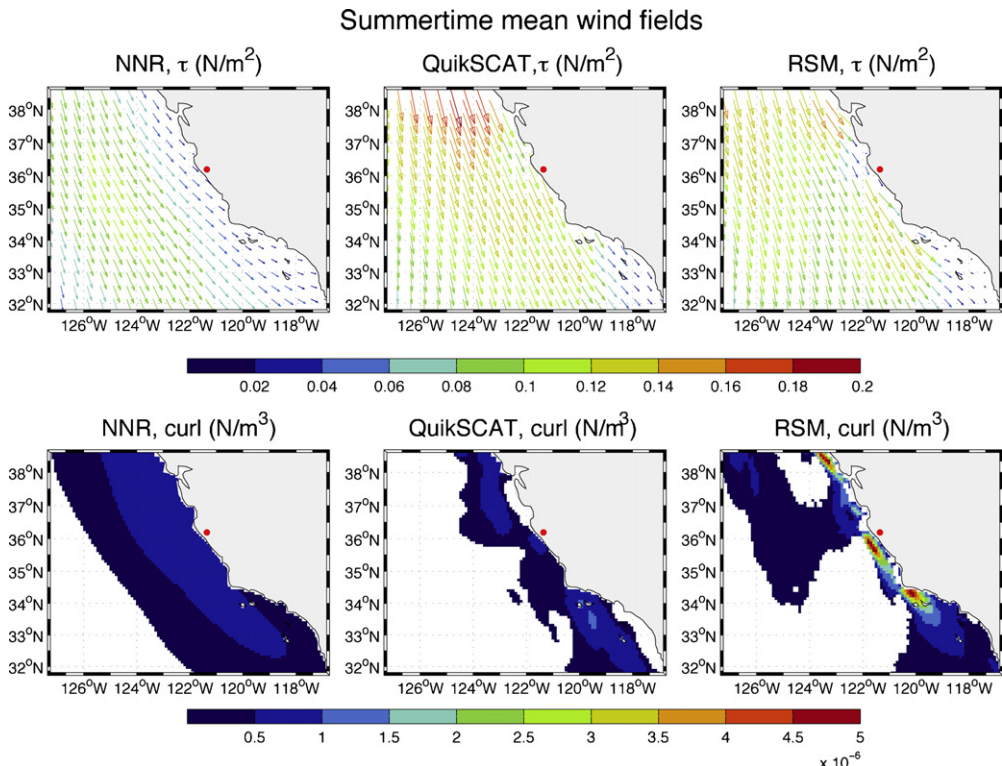


**Fig. 2.** The summertime mean wind stress (top) and wind stress curl (bottom) from NCEP/NCAR Reanalysis (left), gridded QuikSCAT (middle) and downscaled RSM (right). Only the positive values of wind stress curl are shown at the bottom panels so the white regions indicate either zero or negative curl. The strength of the wind stress is indicated by the color of the vectors, and red dot is the location of Point Sur.

the ROMS adjoint model with passive tracers to show that the upwelling cell depth for the cold phase of Pacific Decadal Oscillation is deeper than that for warm phase of Pacific Decadal Oscillation. Following their methods to identify the water sources, we investigate the changes of upwelling source waters under several different wind stress fields in this study.

The paper is organized as follows. First, the dependence of the wind stress curl on the wind forcing resolution is discussed in Section 2. Then Section 3 describes the details of the model setting for the simulation including the adjoint model with passive tracers. Results of the forward model and the upwelling water source for the different wind stress curl regimes are presented in Section 4 and Section 5, respectively, followed by a general discussion to conclude in Section 6.

## 2. Surface wind forcing

Many wind forcing products with various resolutions are available over the CCS region. Among them, we choose three wind forcing products for comparison. Those are the  $2^\circ$  resolution NCEP/NCAR Reanalysis (NNR) (Kalnay et al., 1996),  $0.5^\circ$  resolution QuikSCAT mean wind fields over uniform grid points constructed by CERSAT, at IFREMER, Plouzané (France) and a 10 km resolution Regional Spectral Model (RSM) wind product (Kanamitsu and Kanamaru, 2007) that is dynamically downscaled from NNR.

Summertime mean wind stress and wind stress curl from the three wind forcing products interpolated by bicubic splines to the 9 km grid have different structure and magnitude (Fig. 2). The direction of the wind stress is similar in all three wind forcing products, generally toward the southeast along

the coastline, but the low resolution wind forcing product generally has weaker wind stress than the higher resolution wind forcing product. In particular, the maximum of the wind stress in NNR is about half the value in the other products.

Another obvious difference is the distance of the wind stress maximum from the coast. The NNR has the maximum wind stress about 250 km from Point Sur (red dot in Fig. 2). As the resolution of the wind forcing product increases, the wind stress maximum occurs closer to the coastline—about 80 km from the coast in the QuikSCAT and about 40 km offshore in the RSM.

The location of the wind stress maximum anticipates the wind stress curl field. The bottom panels in Fig. 2 show the regions with positive wind stress curl, which occurs in the area between the coast and the location of the wind stress maximum. The NNR has a broad area of positive wind stress curl, but its magnitude is smaller than the others. The QuikSCAT product has a smaller positive area than the NNR with a similar magnitude of wind stress curl. However, the RSM has the strongest wind stress curl, almost 10 times the maximum of the other two, concentrated near the coastline. This maximum wind stress curl value is comparable to the value from the CalCOFI observations (Winant and Dorman, 1997) and from 9 km resolution COAMPS (Capet et al., 2004). Since the positive wind stress curl drives the upwelling via Ekman pumping, the magnitude of the upwelling will be different depending on which wind forcing is used.

The wind forcing also controls the features of the CCS. In the South California Bight, Di Lorenzo (2003) compared three ocean model runs forced by three different wind forcing products— $2^\circ \times 2^\circ$  resolution Comprehensive Ocean-Atmosphere Data Set (COADS),  $1^\circ \times 1.5^\circ$  resolution of NCEP Pacific Ocean Analysis data, and the 10 km resolution RSM reanalysis. He found that the model integration with downscaled RSM reanalysis was able to best reproduce the nearshore recirculation shown in CalCOFI observations.

These differences in wind stress and wind stress curl among three wind forcing products are expected. Since the NNR has a resolution of  $2^\circ$ , there are only two values roughly every 200 km, so all features in the wind forcing less than 400 km, which is twice the grid spacing, will not be resolved. The QuikSCAT product can represent features larger than 100 km, while the RSM can resolve features smaller than 100 km.

In this study, we do not argue that the low resolution wind forcing is inappropriate, but we examine the effect of the location of the wind stress maximum, which determines the wind stress curl field. In particular, we try to answer these two questions—How different is the upwelling as the wind stress maximum moves closer to the coast, and what are the subsurface regions that supply the upwelling water sources? In order to answer the first question, we use the forward model of the CCS under idealized winds. In order to answer the second question, we use the adjoint model of the CCS with a passive tracer.

### 3. Model description

#### 3.1. Model

The ocean model used for the experiments is the Regional Ocean Modeling System (ROMS). It is a split-explicit, free-surface, hydrostatic model with terrain-following vertical coordinate system, solving the primitive equations (Haidvogel et al., 2000, 2008; Shchepkin and McWilliams, 2004). ROMS has been used for many studies over various regions of the North Pacific Ocean, especially the California Current System (Marchesiello et al., 2003; Di Lorenzo, 2003; Capet et al., 2004; Di Lorenzo et al., 2005, 2008; Seo et al., 2007; Veneziani et al., 2009; Broquet et al., 2009). Given the successful simulations of long-term variability of this region, we follow Chhak and Di Lorenzo (2007)'s model configuration.

The model has a one-way nested domain shown in Fig. 3, covering central and southern California coastal areas. The parent domain has 18-km resolution with 30 vertical levels, and its initial and boundary conditions come from the 1999–2004 monthly averaged Estimating the Circulation and Climate of the Ocean (ECCO) analysis whose resolution is  $1^\circ$  (Stammer et al., 2002; Köhl et al., 2007). The ocean states are integrated for 6 years, with the last 5 years considered in these experiments. This parent grid simulation provides the initial and boundary conditions for the child domain with a

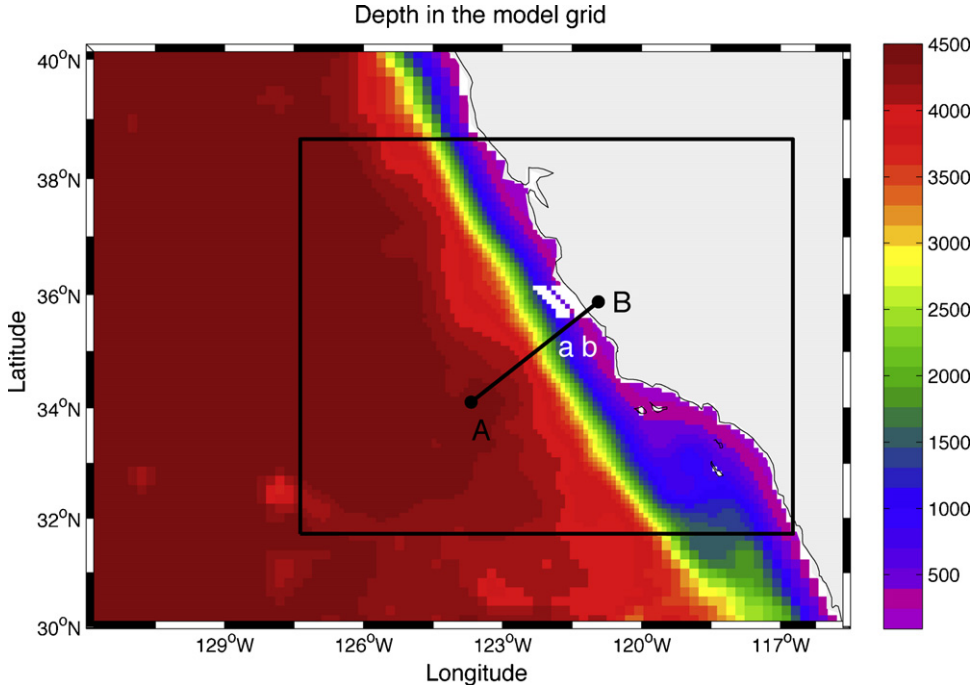


**Fig. 3.** Model domain. 9 km horizontal resolution inner domain (black square) is nested to the outer grid whose horizontal resolution is 18 km. Line A–B represents the cross-shore vertical section line, and white area 'a' and 'b' represent the area where the perturbation of the passive tracer concentration was given.

resolution of 9 km and 30 vertical levels. The surface heat flux and fresh water flux are prescribed from a climatology, with the surface heat flux modified to include a space and time dependent Newtonian damping term that relaxes the model SST to the monthly SST climatology from the National Oceanic and Atmospheric Administration (NOAA) (Smith and Reynolds, 2004). The details are described in Chhak and Di Lorenzo (2007). The surface wind forcing will be discussed in the following subsection.

### 3.2. Idealized wind forcing

In order to isolate the effect of the wind stress curl on the upwelling and its water sources, we first idealize the surface wind forcing based on the features seen in the realistic forcing discussed in Section 2. We create four idealized wind stress fields as shown in Fig. 4(a)–(d). All four have the wind stress parallel to the coastline, with the wind stress at the coastline set to be the same for all of them. The first idealized forcing called “Const” has uniform wind stress over the domain. During the upwelling season (from April to July), the other three forcing fields have the alongshore wind stress  $\tau_a(x)$  in cross-shore direction defined as

$$\tau_a(x) = \begin{cases} a_1 & \text{if } x < -2d \\ \frac{a_2 - a_1}{d}x + (2a_2 - a_1) & \text{if } -2d \leq x < -d \\ -\frac{a_2 - a_3}{d}x + a_3 & \text{if } -d \leq x < 0 \\ a_3 & \text{if } x \geq 0 \end{cases}, \quad (1)$$

where  $d$  is the distance from the coast to the wind stress maximum,  $a_1$  is the offshore wind stress,  $a_2$  is the wind stress maximum and  $a_3$  is the wind stress at the coast. The cross-shore wind stress  $\tau_c$  is

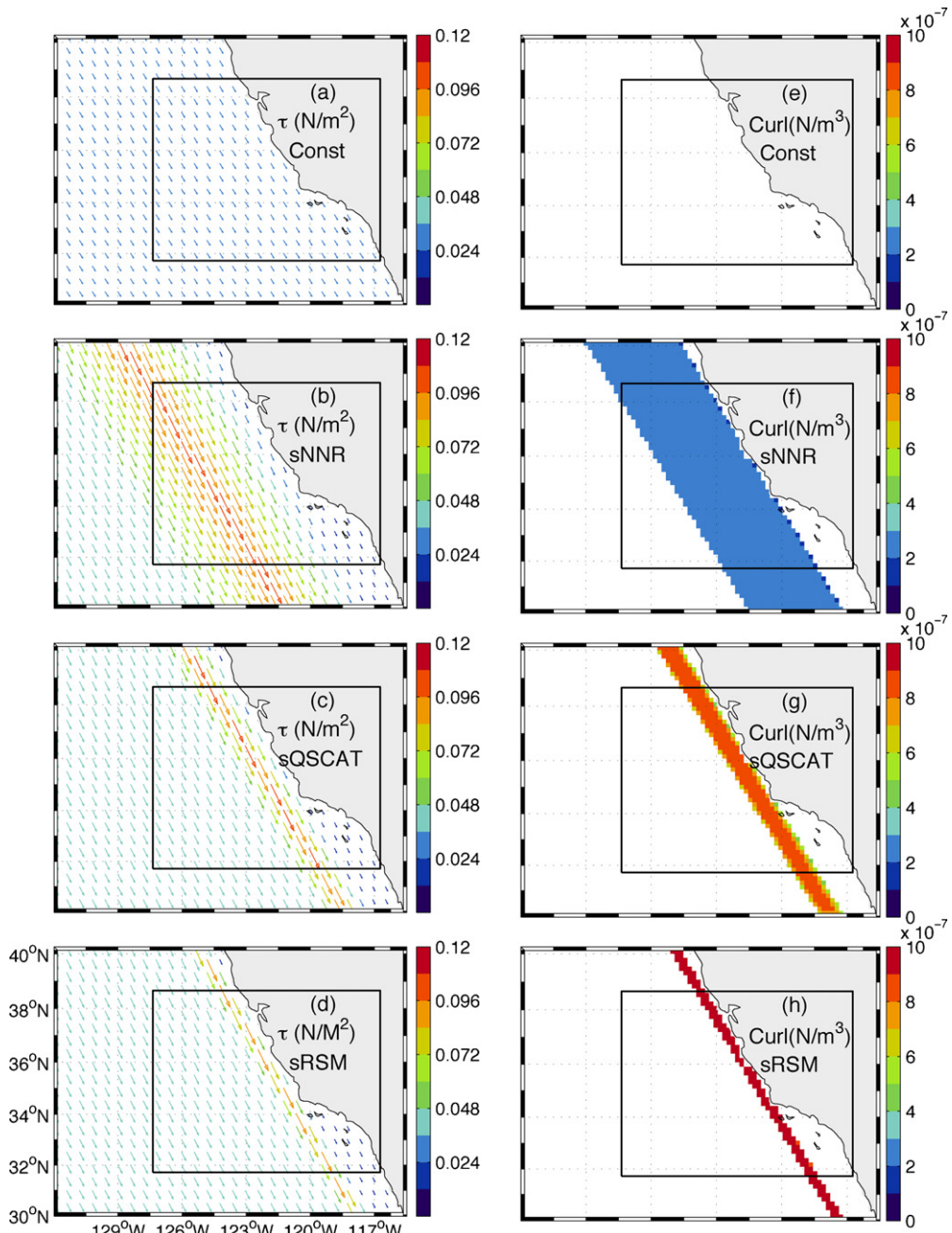


**Fig. 4.** Four idealized wind stress fields (a–d) and the wind stress curl fields (e–h) during the upwelling season. Both color and length of the arrow in the wind stress fields (a–d) represent the magnitude of the wind stress. Const has an uniform wind stress, and sNNR, sQSCAT and sRSM have a cross-shore variability in wind stress. The maximum wind stresses set to be the same, but the distances from the coast vary. In the wind stress curl fields (e–h), only positive values are shown in color, and areas of negative or zero wind stress curl are masked with white. Black boxes represent the inner grid.

**Table 1**

Estimated maximum Ekman pumping vertical velocity using the maximum wind stress curl values in the three idealized wind forcing fields.

		sNNR	sQSCAT	sRSM
Max. wind stress curl, $\nabla \times \tau$	( $\mu\text{N}/\text{s}^3$ )	0.24	0.85	1.70
Max. Ekman pumping velocity	( $\mu\text{m}/\text{s}$ )	2.82	9.91	19.84
	( $\text{m}/\text{day}$ )	0.24	0.86	1.73

zero everywhere, and the wind stress is rotated by  $31.5^\circ$  to be approximately parallel to the coast line. Over the ocean ( $x < 0$ ), the wind stress maxima ( $a_2$ ) are set to be the same in all three forcing fields, but at different distances from the coast. In these experiments, the parameters  $a_1$ ,  $a_2$  and  $a_3$  are set to be  $0.04 \text{ N m}^{-2}$ ,  $0.1 \text{ N m}^{-2}$  and  $0.02 \text{ N m}^{-2}$ , respectively. The locations of the wind stress maxima,  $d$ , are 350 km, 100 km and 50 km offshore based on the NNR, QuikSCAT, and RSM. The idealized products are labeled as simulated NNR or “sNNR”, simulated QuikSCAT or “sQSCAT” and simulated RSM or “sRSM”, respectively. All of them have an identical seasonal cycle in amplitude: the wind stress is reduced by a factor of 1/2 after the upwelling season, and becomes zero during the winter (from November to January). Then the wind stress linearly increases to the upwelling season values during the early spring.

Fig. 4(e)–(h) shows only the positive wind stress curl for the four idealized wind forcing fields, so the white areas offshore have either negative or zero wind stress curl. As expected, wind stress curl is zero in Const. The other wind stress curl fields are determined by the location of the wind stress maximum. In the sNNR, a broader area has positive wind stress curl, but the magnitude is the weakest among the idealized wind forcing products. sQSCAT has stronger positive curl than sNNR, but over a narrower area. The sRSM has the strongest positive wind stress curl, almost five times stronger than sNNR, but the positive curl areas are the smallest and they are near the coastline.

Given the wind stress curl, we can estimate the Ekman pumping velocity (EPV) (Gill, 1982) assuming that the divergence of water transported laterally by wind stress should be balanced by vertical transport.

$$w = \frac{1}{\rho_s f} \mathbf{k} \cdot (\nabla \times \tau), \quad (2)$$

where  $\rho_s$  is seawater density,  $f$  is the Coriolis parameter and  $\mathbf{k} \cdot (\nabla \times \tau)$  is the vertical component of the wind stress curl. Table 1 shows the maximum of the positive wind stress curl and its corresponding EPV for each idealized wind forcing. Shifting the wind stress maximum close to the coastline increases the wind stress curl and EPV. The largest EPV comes from the sRSM:  $1.984 \times 10^{-5} \text{ m s}^{-1}$ . For comparison, Winant and Dorman (1997) estimated the maximum EPV over the Southern California Bight (SCB) as  $4 \times 10^{-5} \text{ m s}^{-1}$  using CalCOFI observation.

### 3.3. Adjoint model with passive tracer

Although adjoint models are widely used in variational data assimilation (Derber, 1985; Lewis and Derber, 1985; Le Dimet and Talagrand, 1986; Thacker, 1989), they are also “powerful tools for many studies that require an estimate of sensitivity of model output with respect to input” (Errico, 1997). The adjoint model integrates the sensitivity of a quantity to perturbations backward in time, so the output is the sensitivity of that quantity to all state variables at all timesteps (Moore et al., 2004). In other words, the adjoint model simply yields the sum of all the Green’s function corresponding to the quantity. It is worth noting that the sensitivity test using the adjoint model is valid only if the linear approximation holds.

We consider here the linear function  $J$  defined as the sum of scalar quantity  $J_i$  over the time range ( $t_n \leq t_i \leq t_N$ ),

$$J = \sum_{i=n}^N J_i = \sum_{i=n}^N \mathbf{h}_i^T \mathbf{x}(t_i), \quad (3)$$

where  $\mathbf{x}(t_i)$  is a vector with control variables that can include external forcing and open boundary conditions, and  $\mathbf{h}_i$  is a vector that relates the state variables to the function  $J_i$  at time  $t_i$ . Under the linear approximation, a small perturbation  $\delta\mathbf{x}$  to  $\mathbf{x}$  can be integrated by the tangent linear model  $\mathbf{M}$  that is the first order approximation of that full nonlinear model. Hence  $\delta\mathbf{x}(t_i)$  can be written as

$$\delta\mathbf{x}(t_i) = \mathbf{M}(t_0, t_i)\delta\mathbf{x}_0 \quad (4)$$

using a tangent linear model  $\mathbf{M}(t_0, t_i)$  that integrates  $\delta\mathbf{x}_0$  from  $t_0$  to  $t_i$ . Then the sensitivity of  $J_i$  to  $\delta\mathbf{x}_0$  can be expressed using the adjoint model operator  $\mathbf{M}^T$ ,

$$\frac{\partial J_i}{\partial \mathbf{x}_0} = \mathbf{M}^T(t_i, t_0)\mathbf{h}_i. \quad (5)$$

Therefore, the total sensitivity is

$$\frac{\partial J}{\partial \mathbf{x}_0} = \sum_{i=n}^N \mathbf{M}^T(t_i, t_0)\mathbf{h}_i. \quad (6)$$

It is computationally effective when only the sensitivities of  $J$  with respect to all other control variables are needed, because this requires only a single integration of the adjoint model. Since it is valid only if the assumption of linearity holds, a long integration of the adjoint model can be prohibited by nonlinearity in the model, and a linearity test is usually done prior to adjoint experiments.

If we consider  $J$  as a measure of perturbation of the concentration of passive tracers, the results from the adjoint model can be interpreted as the source water. The passive tracer without sources and sinks evolves in time following

$$\frac{\partial C}{\partial t} = -\mathbf{u} \cdot \nabla C + \nabla \cdot \kappa \nabla C, \quad (7)$$

where  $C$  is the passive tracer concentration,  $\mathbf{u}$  is the three-dimensional velocity with components  $(u, v, w)$ , and  $\kappa$  is the diffusion coefficient. Since the passive tracers only move via advection and diffusion in the absence of the sources and sinks, high sensitivity means that changes in passive tracer concentration in the past are able to induce perturbations of  $J$ . The adjoint model with passive tracers is valid for infinite time because the passive tracers evolve linearly in time as in (7).

In these experiments, we define  $J$  as the passive tracer concentration (like injecting the passive tracer in the adjoint model) in two different boxes over the shelf. The first box (a) extends from 36 to 63 km offshore and 63 km in alongshore direction near the Point Sur. The second box (b) extends from the coast to 36 km offshore and 63 km in alongshore direction near the Point Sur. These boxes are marked in white with letters 'a' and 'b', respectively in Fig. 3. The onshore and offshore passive tracer are meant to track the source waters of coastal upwelling and open ocean upwelling, respectively. Passive tracer is injected at the top three levels which range from the surface down to  $-10$  m depth and for 15 days at the end of the upwelling season (July) in order to average over the effects of any specific eddies. Hence, the  $\mathbf{h}_i$  in (3) is a vector with 0 elements except for the elements corresponding to the passive tracer within the areas 'a' or 'b' whose values are 1, and  $J = \sum_{i=(N-n)}^N J_i$ , where  $N$  corresponds to the end of July and  $n$  is 15 days, is the sum of all passive tracer concentration in the target region. Hence,  $J$  is the 15 day integral of tracer concentration over the two target regions 'a' and 'b'. The adjoint model is integrated backward in time for 4 months during the upwelling season from July to April. This 4-month adjoint experiment with adjoint forcing during the last 15 days of July is repeated for each of the 5 years, and the sensitivity results are averaged over all cases.

#### 4. Upwelling in the forward model

##### 4.1. Sea surface

During the upwelling season, the four months from April to July, we force the ocean with the idealized steady wind stress shown in Fig. 4, and the resulting mean sea surface height (SSH), surface current and sea surface temperature (SST) are shown in Fig. 5.

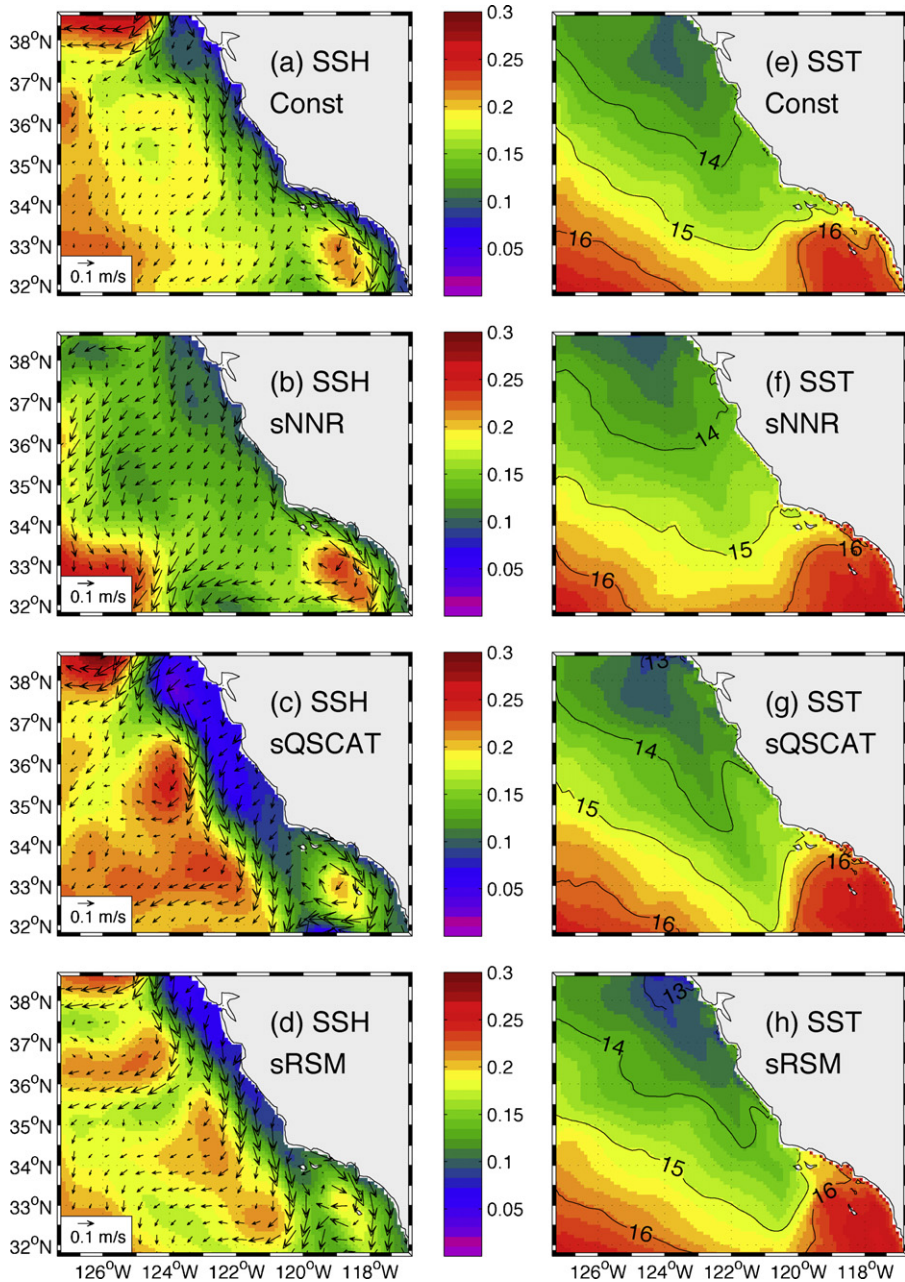


**Fig. 5.** Upwelling season mean sea surface height with surface current in arrows (a–d) and mean sea surface temperature (e–h) in four cases.

The SSH and the surface current in Fig. 5(a)–(d) shows two main features. First, offshore transports are observed over much of the domain in all cases as a result of Ekman transport. Second, the equatorward currents are present in all cases although their spatial distribution differs. Without wind stress curl (Fig. 5(a)), the core of the equatorward current can be found near the coast. As the wind stress

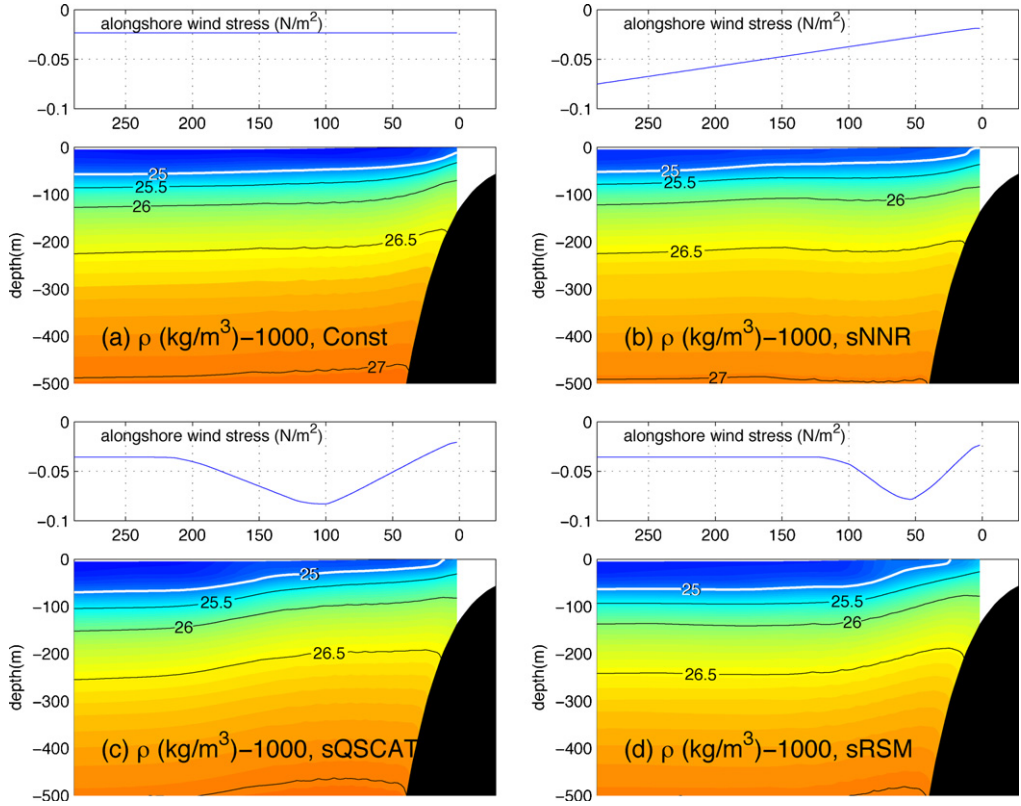


**Fig. 6.** Upwelling season mean cross-shore vertical profiles of alongshore wind stress and density along the line A–B in Fig. 3 in four cases. Negative wind stress means the equatorward.

curl field changes, the location of the core of the equatorward flow also changes, and moves closer to the coast as the wind stress maximum approaches the coast. The positive and negative wind stress curl leads to divergence and convergence of the surface water, respectively. As a result, SSH under the positive (negative) wind stress curl is lower (higher) than the SSH field with no wind stress curl in Fig. 5(a). This modifies a cross-shore SSH gradient, resulting changes in location of an equatorward geostrophic current. Hence, the location of the core of the equatorward flow depends on the wind stress curl fields.

SST looks very similar in all cases. This is because the climatological surface heat flux is modified to force the model to follow the monthly NOAA SST. Although the contours of the isotherms appear to be affected by the surface current, the effect of wind forcing on the upwelling is obscured by the SST nudging. In a separate simulation without the nudging term in the heat flux calculation, the SST fields show that the coastal upwelling by the Ekman transport occurs only in a narrow region near the coast, with stronger upwelling occurring as the wind stress maximum approaches the coast (not shown). However, since the specified (non-interactive) surface heat flux can induce a modification of the surface current in the cases where SST deviated strongly from climatology, we choose to incorporate the SST nudging for these experiments to keep SST close to climatology.

#### 4.2. Vertical section

The vertical sections of density in Fig. 6 are useful to discuss the relation between the upwelling rate and the resolution of the wind product. The upper small panels in Fig. 6 shows the cross-shore

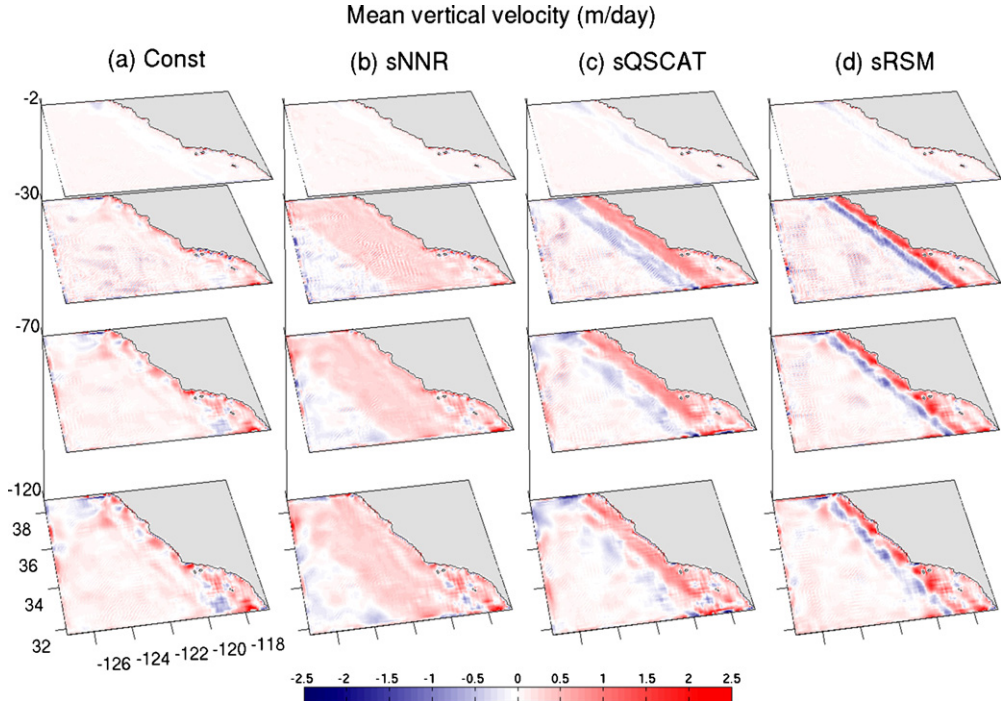


**Fig. 7.** Three-dimensional upwelling season mean vertical velocity at from  $-2\text{ m}$  to  $-120\text{ m}$  depth in four cases. Positive (negative) shown in red (blue) represents upward (downward) vertical velocity.

profile of the alongshore wind stress. Wind stress values are negative, meaning equatorward as shown in Fig. 4. Lower panels show vertical sections of the upwelling season mean density from the surface to  $-500\text{ m}$  depth along the cross-section A–B in Fig. 3.

The density vertical sections show stronger coastal upwelling with higher resolution wind forcing. In the sQSCAT and sRSM case (Fig. 6(c) and (d)), the  $\sigma = 25\text{ kg m}^{-3}$  isopycnal outcrops at the surface, but not in the Const and sNNR (Fig. 6(a) and (b)). Although several factors (i.e. mixing) determine the isopycnals, Ekman pumping changes in isopycnal depth by lifting and depressing it with positive and negative wind stress curl, respectively (Gill, 1982). This is observed not only near the surface but also in the interior of the ocean. The isopycnal displacements might indicate a different rate of upwelling at the coast. In the sNNR case, the gradient of the cross-shore 25 isopycnal is more gradual than in either sQSCAT or sRSM case, resulting in the shallower and slower coastal upwelling. As the wind stress maximum approaches to the coast, the cross-shore gradient of the isopycnal depth becomes steeper because of both the proximity and the strength of the positive and negative wind stress curl. Hence, we can expect the upwelling is the fastest and deepest in the sRSM case.

This is supported by Fig. 7 that shows the vertical velocity averaged over the upwelling season in four cases. Although pressure gradient error due to the terrain-following coordinate in ROMS can add undesired features to the vertical velocity field, the mean vertical velocity is positive (upward) along the coast as a result of the coastal upwelling in all cases. It is also upward under the positive wind stress curl, while the negative wind stress curl drives downward vertical velocity as a result of Ekman pumping. The intensity of the vertical velocity is closely related to the strength of the wind stress curl according to (2), and this relation is well observed in the model, too. The upward vertical velocity in all cases is faster than the EPV (Table 1).

Fig. 8 shows the vertical section of alongshore current in four different cases. Blue and red colors mean equatorward and poleward, respectively. Three main features can be pointed out from the

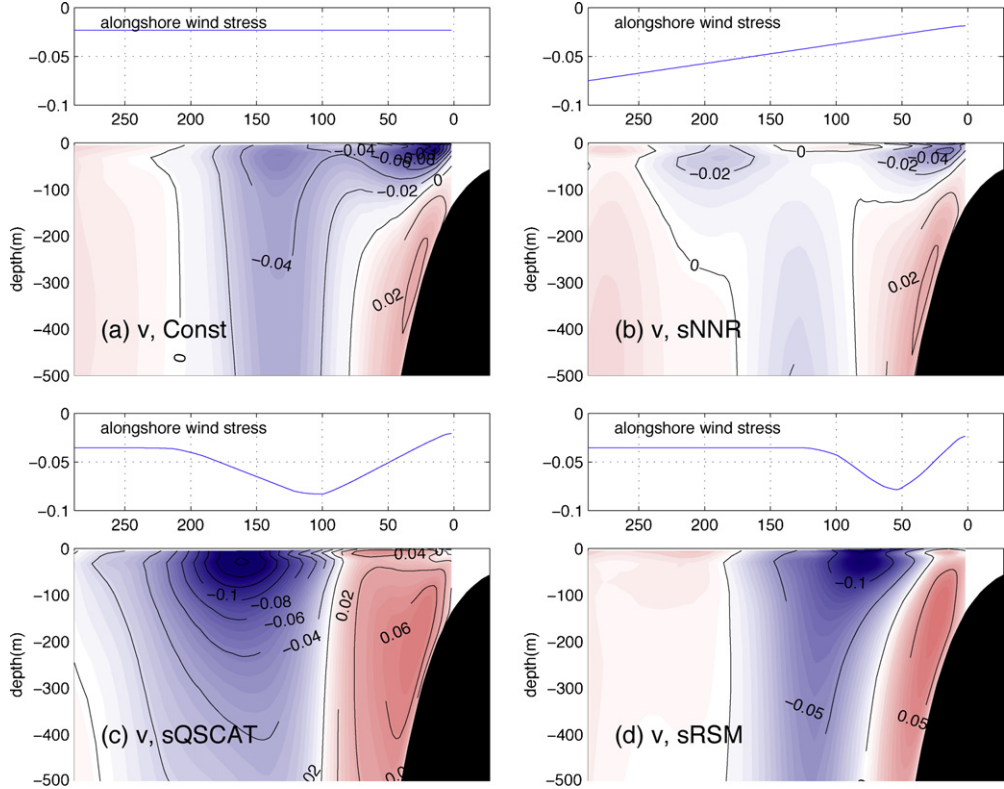


**Fig. 8.** Upwelling season mean cross-shore vertical profiles of alongshore wind stress and alongshore current along the line A–B in Fig. 3 in four cases. Negative values in alongshore current (blue) mean equatorward and positive values (red) mean poleward.

alongshore current vertical section. First, we observe an equatorward surface current in all cases, although the locations are different. As discussed in Section 4.1, the core of the equatorward flow depends on the location of the wind stress maximum. Without the wind stress curl in Const case, the core of the equatorward flow is very close to the coast (within 50 km). In the other cases, the location of the core of the equatorward flow gets closer to the coast as the wind stress maximum shifts to the coast (Fig. 5(a)–(d)). Although it is not seen in this figure, sNNR has equatorward flow farther than 250 km offshore as well as near the coast as shown in Fig. 9, which is the mean current fields with depth during the upwelling season. However, the strength of the equatorward flow is not related to the strength of the wind stress curl. Second, there is a surface poleward current under the positive wind stress curl, and an equatorward surface current under the negative wind stress curl. This is more obvious when the magnitude of the curl is stronger (Fig. 8(c) and (d)). Last, the poleward undercurrent on the continental slope is present in all cases, even when there is no curl. The poleward flow is partially due to the open boundary conditions from ECCO and is present even in case with no wind forcing (not shown).

These results are consistent with previous research. McCreary et al. (1987) saw both an equatorward flow and a poleward undercurrent when the wind forcing has no curl in their model solutions, supporting the idea that wind stress curl does not drive the undercurrent. When they included curl in the wind forcing, they saw a poleward surface current near the coast, and an equatorward current farther offshore. This can be explained by the Sverdrup balance, which has northward transport under the positive wind curl, and equatorward transport under the negative curl.

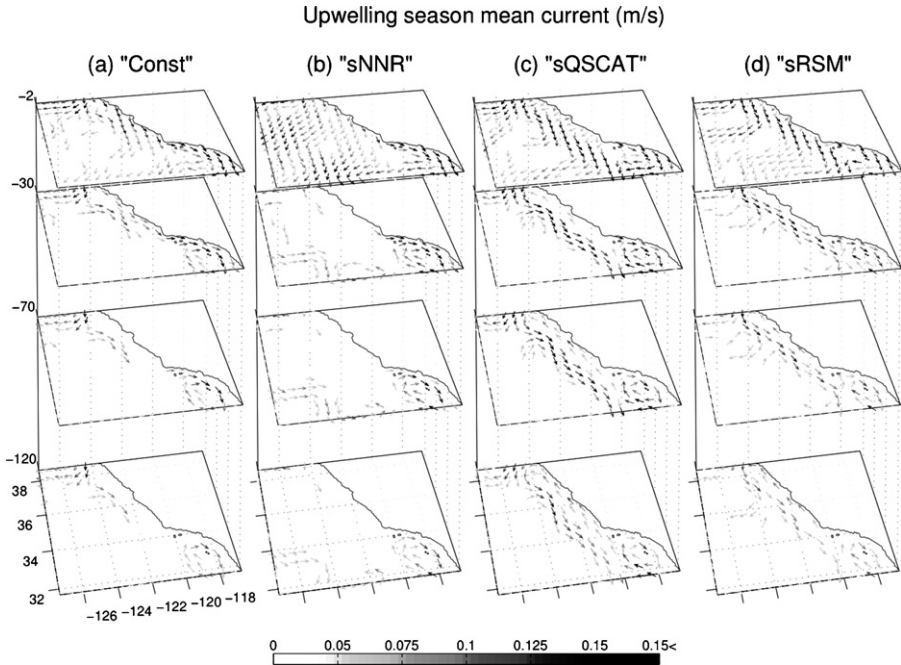


**Fig. 9.** Three-dimensional upwelling season mean current at from  $-120\text{ m}$  to  $-2\text{ m}$  depth in four cases. Arrows representing current weaker than  $0.05\text{ m s}^{-1}$  are in white and, hence, invisible.

## 5. Upwelling water source

In order to identify the upwelling source waters, we introduce perturbations into the adjoint passive tracer equation at the end of July each year from the surface to  $-10\text{ m}$  in the areas of interest labelled as ‘a’ and ‘b’ in Fig. 3, and run the adjoint model for four months backward during the upwelling season in each of the last 5 years of the forward run. Then we average the adjoint model solutions from each year and explore the upwelling source waters for the coastal and offshore passive tracer patches under the four different idealized wind forcing scenarios.

Figures from 10 to 13 show the three-dimensional view of the 5-member ensemble mean of 4-month adjoint model runs. The colors in the figures show the  $\log_{10}((1/J)\partial J/\partial \mathbf{x}(t_i))$ , where  $J$  is the sum of all passive tracer concentration for the last 15 days of July in the top three levels of the white area shown in Fig. 3 as explained in Section 3.3. This represents the normalized sensitivities of  $J$  to the passive tracer concentrations at other areas at previous times over the 4-month period. For example, if the  $\log_{10}$  sensitivity at a certain grid point at time  $t_i$  is  $-2$ , the total cost function  $J$  can be increased by 1% with a perturbation of 1 at that grid point at time  $t_i$ . Each figure has two rows and four columns. The top and bottom rows show the results for perturbations initiated at the onshore and offshore locations, respectively. The columns show the snapshot of the adjoint model results at every month at different depths. Since the adjoint model integrates the sensitivity backward in time, the results of the adjoint model runs were plotted from July (left) to April (right) with one month interval.

The sensitivities for passive tracers can be interpreted as the source waters because sensitivity results only from advection and diffusion, unless there are sources or sinks, as discussed in Section 3.3. Thus the “sensitivity” of the passive tracer concentration will henceforth be called the passive tracer “concentration”.

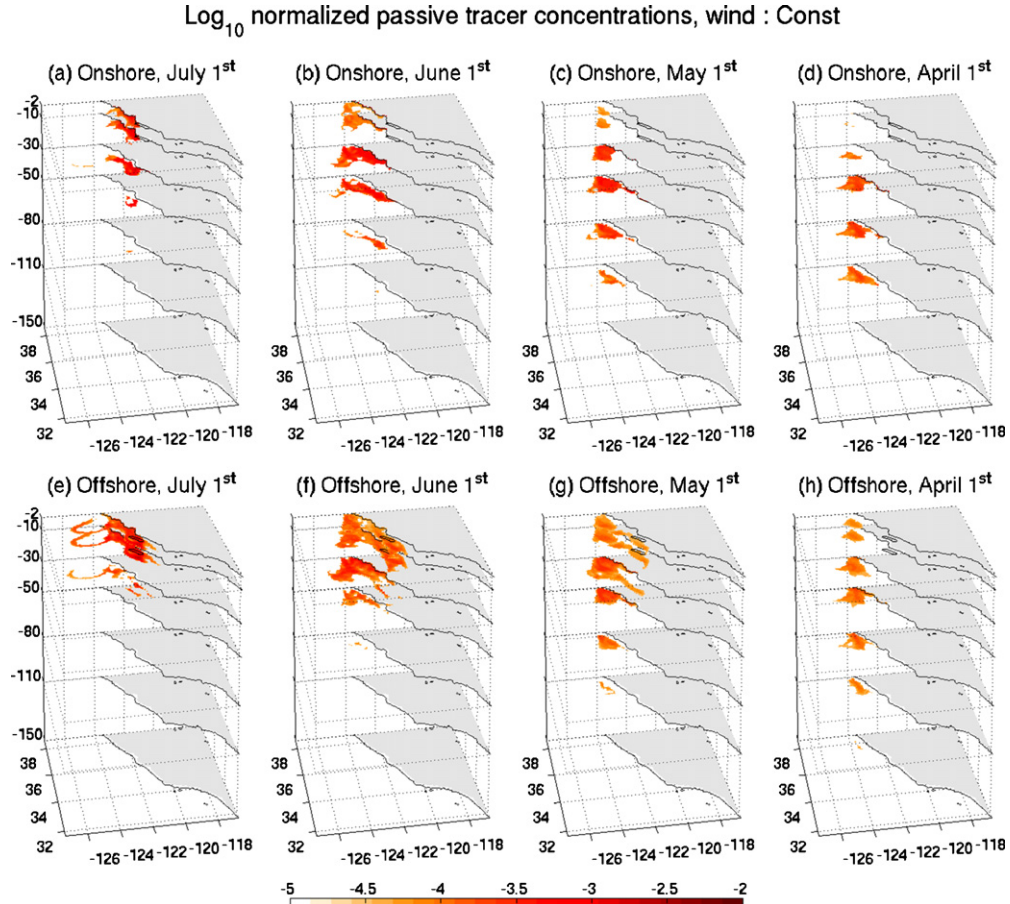


**Fig. 10.** Normalized sensitivity of passive tracer concentration in logarithmic scale when the Const forced the ocean. Top row (a–d) shows the four-month time series of passive tracer concentration sensitivity backward in time when the initial perturbations of passive tracer were defined in 'b' in Fig. 3. Bottom row (e–h) shows the same four-month time series, but when the initial perturbations were defined in 'a' in Fig. 3.

### 5.1. Coastal upwelling source water

In each case, vertical advection is the significant process for July coastal upwelling. Although vertical advection is obscured by the equatorward surface advection in Const (Fig. 10(a)) and sNMR (Fig. 11(a)), and by the poleward subsurface advection in sQSCAT (Fig. 12(a)) and sRSM (Fig. 13(a)), it is evident that the vertical advection plays an important role by the small patch of passive tracer concentration deeper than  $-10$  m depth below the area where the tracer is injected (black contour at the top two levels in the subplots from (a) to (d) in Fig. 10 to 13 and white area (b) in Fig. 3). This is the time when the direct effect of the wind on the passive tracer distribution is the strongest. The horizontal advection in Const appears as important as the vertical advection as considerable source waters are found in the north. The horizontal advection from the north in Const and sNMR is by the equatorward flow along the coastline, while sQSCAT and sRSM have the source water coming from the south due to the influence of subsurface poleward flow along the coast (Fig. 8). The speed of the vertical advection increases with stronger wind stress curl as seen in Fig. 7. Const and sNMR have upwelling speeds less than about 1 m/day in general, while the upwelling speeds in sQSCAT and sRSM are greater than 1 m/day for July. The depth from which water is being upwelled to the upper  $-10$  m in July is consistent

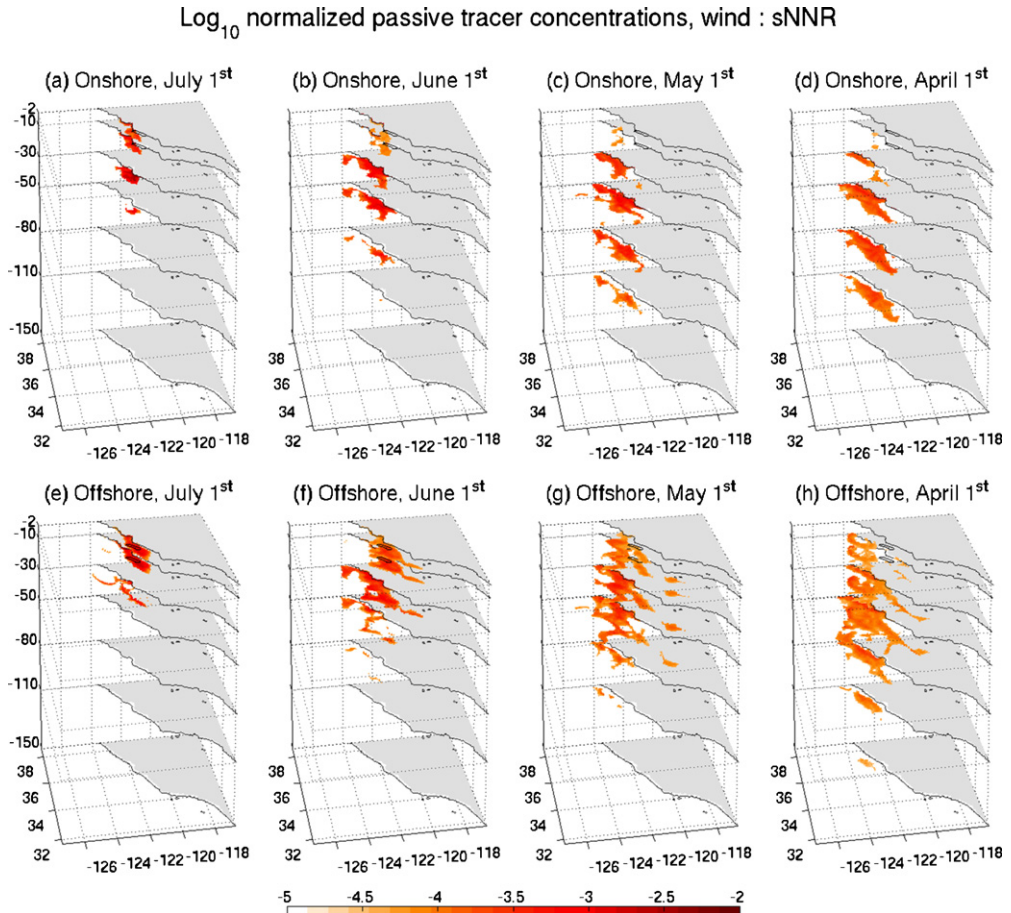


**Fig. 11.** Same as Fig. 10 when the sNMR forced the ocean.

with the theoretical Ekman layer depth, which ranges from 26 m under the weakest wind to 55 m under the strongest wind at 36° N if the sea water density, air density and the drag coefficient are assumed to be 1027 kg/m<sup>3</sup>, 1.25 kg/m<sup>3</sup> and  $2.6 \times 10^{-3}$ , respectively (Stewart, 2005).

Earlier in the upwelling season, horizontal advection and diffusion become important mechanisms affecting the coastal upwelling water sources, and Figs. 8 and 9 are useful to explain the distribution of the upwelling water sources. In Const (Fig. 10), the upwelled water is transported from the north at  $-110 \text{ m} \sim -30 \text{ m}$  depth by the strong equatorward flow ( $>0.1 \text{ m s}^{-1}$ ) near the coast (Figs. 8(a) and 9(a)). As a result, only about 30% of the initial passive tracers remained inside of the domain as seen in Table 2, which shows the percentage of the passive tracer found inside of the domain at the first day of each month. sNMR has the weakest advection, and most of the coastal upwelling water sources are local, showing the highest percentage of the passive tracer left inside of the domain at April 1st, which is the end of the adjoint run (Table 2). This is because the core of the equatorward flow occurs more than 250 km from the coast, and there is no strong current at the surface and subsurface near the coast to affect the upwelling water source (Fig. 9(b)). Although both Const and sNMR have the poleward undercurrent deeper than  $-120 \text{ m}$  (Fig. 8(a) and (b)), it does not affect the upwelling water sources because the upwelling cell is shallower than  $-120 \text{ m}$ . sQSCAT in Fig. 12 has coastal upwelling water sources both from the south and the north at the subsurface. The distribution of the passive tracer concentration reflects the subsurface equatorward flow at about 150 km from the coast and

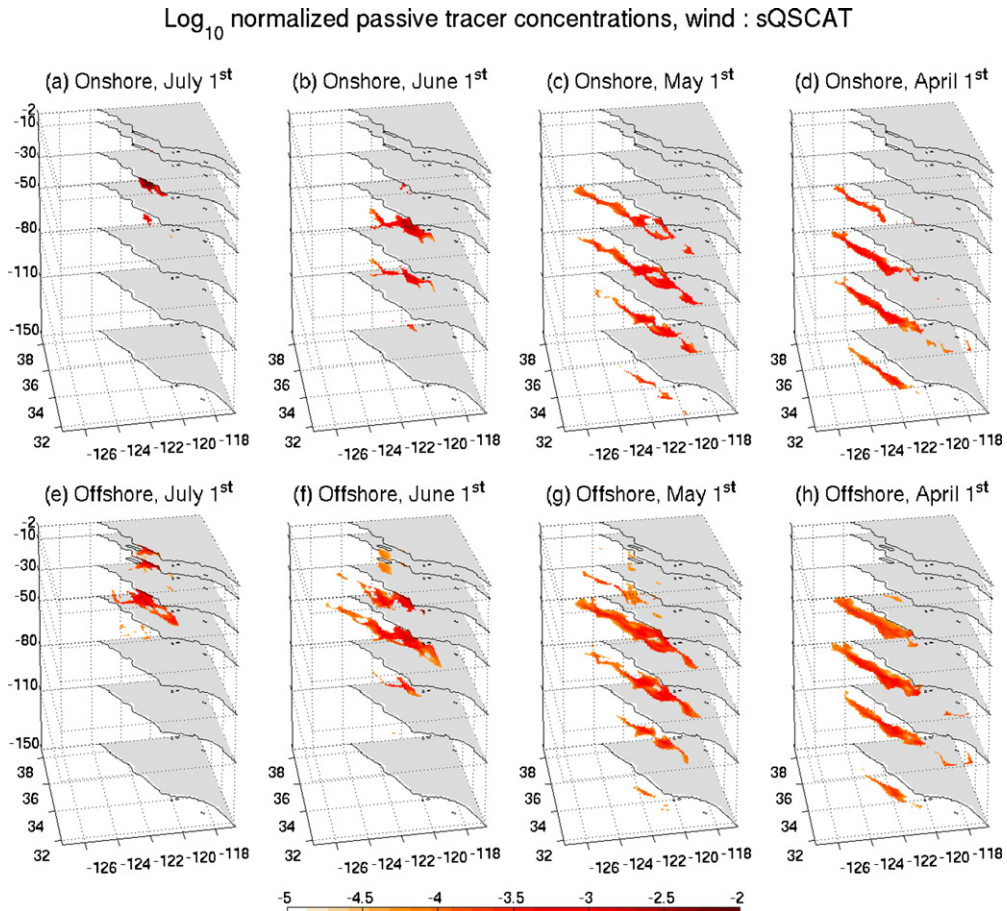


**Fig. 12.** Same as Fig. 10 when the sQSCAT forced the ocean.

subsurface poleward flow along the coast (Figs. 8(c) and 9(c)), supporting the idea that the subsurface flows play the most important role in determining the water sources. High sensitivity at  $-50\text{ m}$  depth near Pt. Conception in Fig. 12(b) indicates that the mixing of two flows occurs at the south of the key area. Then it is transported to the north and upward at the same time. Thus the upwelling water may mix the characteristics of water both from the south and the north. The passive tracer concentration in sRSM in Fig. 13 also reflects the subsurface equatorward flow with the core at about  $75\text{ km}$  from the coast (Figs. 8(d) and 9(d)), which implies strong horizontal advection from the north as well as the

**Table 2**

Percentage (%) of the passive tracer remained in the domain.

		July 1st	June 1st	May 1st	April 1st
Onshore	Const	100	89.00	52.62	31.44
	sNNR	100	99.47	89.21	80.91
	sQSCAT	100	99.91	93.64	74.15
	sRSM	100	93.75	70.80	53.38
Offshore	Const	99.94	82.49	49.69	29.25
	sNNR	100	96.10	85.96	79.84
	sQSCAT	100	98.66	89.70	72.75
	sRSM	99.53	86.80	68.28	56.78

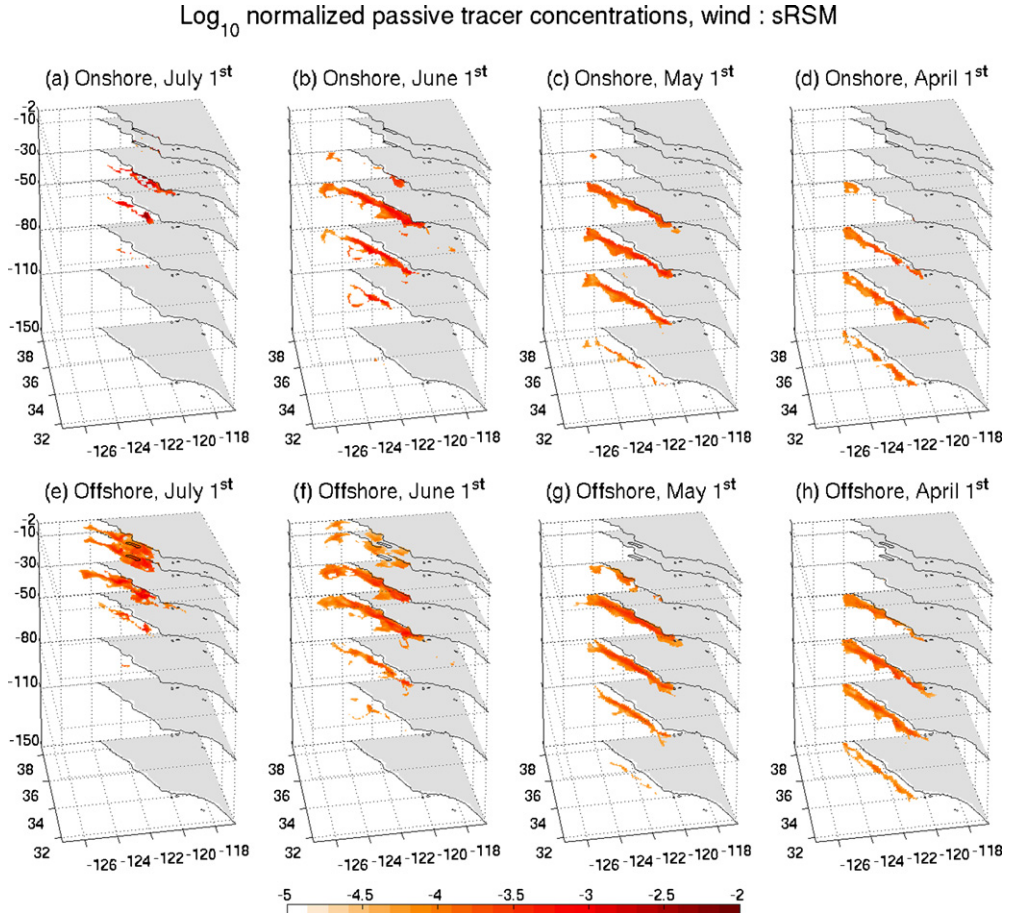


Fig. 13. Same as Fig. 10 when the sRSM forced the ocean.

subsurface poleward transport. As will be more evident from the results of Section 5.2, the upwelling cell in both sQSCAT and sRSM is deeper than in the other two cases. This means that the poleward undercurrent can bring water from the south toward the areas of interest.

Four months earlier (April), the depth of the coastal upwelling cell exhibits a dependence on the strength of the wind stress curl. The subplot (d)s in Figs. 10–13 show the tendency of a deepening coastal upwelling cell with stronger curl. In Const, the upwelling cell is shallower than  $-150\text{ m}$ , but it is deeper than  $-150\text{ m}$  in sRSM. As seen in Fig. 7, sRSM has the strongest upward velocity near the coast due to the strongest positive wind stress curl. Thus, the upwelling is the fastest and the upwelling cell is the deepest among four cases. In contrast, sNRR has broad areas of upward velocity, but the intensity is less than half of that in sRSM. This is also reflected by the cross-shore isopycnal gradient discussed in Section 4. Const and sNRR have flat isopycnals near the coast (Fig. 6), indicative of their upwelling cells being shallower and more diffusive than sQSCAT or sRSM. The strongest positive and negative wind stress curl near the coast and their proximity make the cross-shore isopycnal gradient in sRSM the greatest, providing the circumstances for the deepest upwelling cell.

## 5.2. Offshore upwelling source water

Unlike the case for coastal upwelling, the lateral transport at the surface is one of the important mechanisms that supply water to the area ‘a’ in Fig. 3 in July as well as at the subsurface shallower

than  $-50$  m in all cases. Const and sNNR show similar water sources for coastal upwelling as the lateral transport from the north is dominant, although their source waters for the offshore patch are shallower. sNNR obviously shows Ekman pumping as the passive tracer patch is found at  $-30$  m depth immediately below the initial offshore passive tracer injection area (Fig. 11(e)). Both sQSCAT and sRSM should have offshore upwelling, but it is not clearly observed in Figs. 12(e) and 13(e) because onshore lateral transport at the subsurface is also significant (not shown).

During April and June, lateral transport has more importance than in July in determining the horizontal distribution of the passive tracer patches. In Const (Fig. 10), most of water sources come from the north from the surface to  $-110$  m depth, reflecting the equatorward flow near the coast (Figs. 8(a) and 9(a)). Similar to the case for coastal upwelling, more than 70% of the passive tracers came from outside of the domain in April 1st (Table 2). The source waters in sNNR also can be found from the surface to  $-110$  m depth. However it has a weaker equatorward alongshore current near the coast than Const. As a result, about 80% of the passive tracer remains inside of the domain at the end of 4-month adjoint model run. sQSCAT and sRSM have very similar water sources for the area 'a' and 'b' in Fig. 3, although more concentration can be found at shallower depth. Fig. 12(h) shows that subsurface water is transported both from the north and the south along the equatorward flow offshore and along poleward flow near the coast for sQSCAT case. This is very similar to the water sources map for coastal upwelling in Fig. 12(d). sRSM also shows very similar water sources for coastal upwelling and offshore upwelling as seen in Fig. 13(d) and (h), reflecting the major role of the equatorward flow.

As expected, the offshore passive tracer patches have water sources shallower than the onshore patches in all cases. There is still a tendency that strong wind stress curl deepens the upwelling water sources. The water at  $-150$  m can reach the surface in both sQSCAT and sRSM case, but Const and sNNR cannot bring up water at  $-150$  m depth to the surface in 4 months (subplot (h)s in Figs. from 10 to 13). This is also consistent with the upwelling season mean vertical velocity in Fig. 7, which shows the strongest vertical velocity in sRSM.

## 6. Discussion

We considered the effects of different wind forcing datasets on the strength and character of upwelling cells in the California Current System. We focused on idealized versions of three key wind forcing datasets, the NCEP/NCAR Reanalysis, the QuikSCAT, and the regional downscaling via RSM. In these three cases, the upwelling-favorable wind has a different structure that significantly depends on the resolution of the wind forcing product that is being idealized. This also results in sharply different wind stress curl patterns in each case, which mimic structures seen in the real products.

In order to isolate the effect of wind stress curl from coastal Ekman transport on the consequent upwelling, we forced an ocean model with the three idealized wind products during the upwelling season. Our analysis included forward and adjoint simulations to see how changes in ocean states control the source waters, paths, and depths of upwelling cells.

The main result from this paper is the tendency of deepening the upwelling cell with sharp changes in wind stress curl and its effects on the upwelling source waters. This is summarized with the schematic diagram in Fig. 14. The structure of wind forcing changes the location of the core of the equatorward flow. When the wind stress has a variability in space so that wind stress curl is introduced, the location of the equatorward flow core is determined by the wind stress curl, as shown in Fig. 14. The equatorward flow is present under the negative wind stress curl (blue), and the poleward flow under the positive wind stress curl (red), which are consistent with the Sverdrup balance. All cases have a poleward undercurrent, which is specified in the boundary condition. However, the positive wind stress curl strengthens the undercurrent as it drives poleward Sverdrup transport.

A cross-section of isopycnals (black) in Fig. 14 shows that more upwelling occurs with stronger wind stress curl. The positive wind stress curl can lift the isopycnal up, and the negative wind stress curl can deepen it, resulting in a steeper cross-shore gradient. When the positive and negative wind stress curl are strong and close to one another, as in Fig. 14[A], the cross-shore gradient of the isopycnal is steep, indicating a deeper upwelling cell. When the positive curl covers a broad area, as in Fig. 14[B], the gradient of the isopycnal is more gradual, resulting in a shallower upwelling cell. When the equatorward flow is located farther offshore than the area where the water can diffuse in a 4-month period

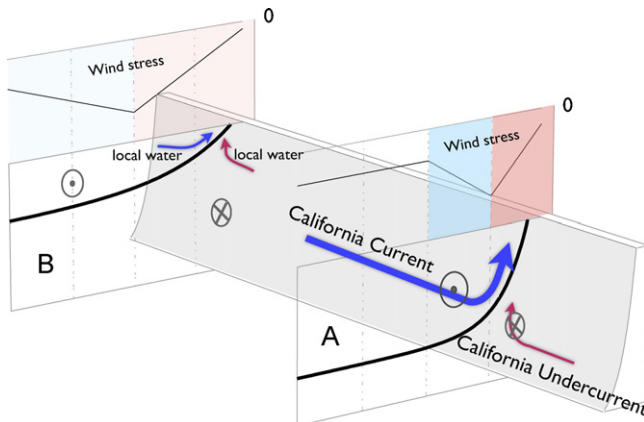


**Fig. 14.** Simplified cartoon to illustrate the relation between the wind stress curl and upwelling and its water sources. Wind stress values are negative meaning equatorward. Corresponding wind stress curl are represented in colors—red for positive wind stress curl and blue for negative wind stress curl. The saturation of the color represents the intensity of the curl. Thick black lines represent the isopycnals. The equatorward flow (circle with dot) can be found under the negative curl, and poleward current (circle with cross) under the positive curl. Blue and red arrows represent the upwelling water sources from the north and the south, respectively.

(Fig. 14[B]), the water sources for coastal upwelling are local. When the equatorward flow is close to the coast (Fig. 14[A]), most of the water sources can be found upstream of the flow. The undercurrent may or may not affect the water sources of the upwelling, depending on the depth of the upwelling cell.

The offshore patch defined here is meant to track the open-ocean upwelling water sources by Ekman pumping. Although there is evidence of Ekman pumping (Fig. 11(e)), onshore and offshore lateral transport make it difficult to distinguish the two Ekman upwelling mechanisms. As a result, the water sources are similar for both coastal and offshore upwelling, especially in the strong wind stress curl cases. The upwelling cell for the offshore patch is generally shallower than the coastal upwelling cell in all cases.

Although these experiments are executed with idealized wind stress fields, they provide insight into the mechanisms that may explain the trends observed in the California Current System. Di Lorenzo et al. (2005) observed a freshening of subsurface water near the equatorward flow with an intensification of the geostrophic current over the last 50 years of the CalCOFI data. In their wind forcing, there was a tendency for wind stress curl strengthening with a positive anomaly nearshore and a negative anomaly offshore. Therefore, the changes in wind stress curl result in more lateral transport from the north as seen in the experiments here, possibly yielding freshening the subsurface water near the core of the flow.

The results from these experiments can also provide some intuition about possible changes in upwelling and its water sources under global warming scenarios. Previous studies (Bakun, 1990; Snyder et al., 2003) anticipate an intensification of upwelling favorable wind and wind stress curl in Eastern boundary current regions with global warming. Thus, in that scenario and based on the experiments here, we can anticipate the following in the CCS; deepening of the upwelling cell, a larger contribution of the California Undercurrent to upwelled water, shifting of the equatorward flow toward the coast and more southward transport by the equatorward flow resulting in freshening the CCS near the core.

This may cause changes in the dissolved oxygen (DO) as the remote areas have more influences on the water characteristics than at present. Bograd et al. (2008) argued that the observed declining trend of DO in the CCS is related to inefficient vertical oxygen transport due to the surface-warming-induced stronger stratification under global warming scenarios. The advection of the consequent low DO water along the California Current from the north, and the advection of historically low DO water along the

California Undercurrent from the south also contribute the observed low DO in the CCS. Thus we may anticipate even lower DO levels in the CCS since the experiments in this study anticipate more remote influence on the CCS upwelling system from both the north and the south. This plausible scenario will be investigated in future work.

## Acknowledgments

This study formed a part of the Ph.D. dissertation of HS at Scripps Institution of Oceanography. Funding was provided by NSF (CCE-LTER: OCE-0417616 and OCE-1026607) and NOAA (IOOS: NA17RJ1231). BDC was also supported by NOAA grant NA17RJ1231 for the Consortium for the Ocean's Role in Climate. The views expressed herein are those of the authors and do not necessarily reflect the views of NOAA or any of its subagencies. Supercomputing resources were provided by COMPAS at SIO. We thank Ketty Chhak for letting us use her model configurations. We also thank Andrew Moore for his advice. The authors would like also to thank two anonymous reviewers for valuable comments and suggestions.

## References

- Bakun, A., 1990. Global climate change and intensification of coastal ocean upwelling. *Science* 247, 198–201.
- Bograd, S.J., Castro, C.G., Di Lorenzo, E., Palacios, D.M., Bailey, H., Gilly, W., Chavez, F.P., 2008. Oxygen declines and the shoaling of the hypoxic boundary in the California Current. *Geophys. Res. Lett.* 35.
- Broquet, G., Edwards, C.A., Moore, A.M., Powell, B.S., Veneziani, M., Doyle, J.D., 2009. Application of 4D-variational data assimilation to the California Current System. *Dyn. Atmos. Oceans* 48, 69–92.
- Capet, X.J., Marchesiello, P., McWilliams, J.C., 2004. Upwelling response to coastal wind profiles. *Geophys. Res. Lett.* 31, 69–92.
- Chan, F., Barth, J.A., Lubchenco, J., Kirincich, A., Weeks, H., Peterson, W.T., Menge, B.A., 2008. Emergence of anoxia in the California Current large marine ecosystem. *Science* 319, 920.
- Checkley, D.M., Barth, J.A., 2009. Patterns and processes in the California Current System. *Prog. Oceanogr.* 83, 49–64.
- Chelton, D.B., 1982. Large-scale response of the California Current to forcing by the wind stress curl. *Calif. Coop. Oceanic Fish. Invest. Rep.* 23, 130–148.
- Chhak, K., Di Lorenzo, E., 2007. Decadal variations in the California Current upwelling cells. *Geophys. Res. Lett.* 34, L14604.
- Derber, J.C., 1985. The variational four-dimensional assimilation of analyses using filtered models as constraints. Ph.D. dissertation, Univ. of Wis., Madison.
- Di Lorenzo, E., 2003. Seasonal dynamics of the surface circulation in the Southern California Current System. *Deep-Sea Res. Pt. II* 50, 2471–2388.
- Di Lorenzo, E., Miller, A.J., Schneider, N., McWilliams, J.C., 2005. The warming of the California Current: dynamics and ecosystem implications. *J. Phys. Oceanogr.* 35, 336–362.
- Di Lorenzo, E., Schneider, N., Cobb, K.M., Franks, P.J.S., Chhak, K., Miller, A.J., McWilliams, J.C., Bograd, S.J., Arango, H., Curchitser, E., Powell, T.M., Riviere, P., 2008. North Pacific Gyre Oscillation links ocean climate and ecosystem change. *Geophys. Res. Lett.* 35.
- Doyle, J.D., Jiang, Q., Chao, Y., Farrara, J., 2009. High-resolution real-time modeling of the marine atmospheric boundary layer in support of the AOSN-II field campaign. *Deep-Sea Res. Pt. II* 56, 87–99.
- Errico, R.M., 1997. What is an adjoint model? *Bull. Am. Meteorol. Soc.* 78, 2577–2591.
- Fukumori, I., Lee, T., Cheng, B., Menemenlis, D., 2004. The origin, pathway, and destination of niño-3 water estimated by a simulated passive tracer and its adjoint. *J. Phys. Oceanogr.* 34, 582–604.
- Gill, A.E., 1982. *Atmosphere-Ocean Dynamics*. Academic Press, San Diego, CA, Ch. 9, p. 662.
- Haidvogel, D., Arango, H., Hedstrom, K., Beckmann, A., Malanotte-Rizzoli, P., Shchepetkin, A., 2000. Model evaluation experiments in the North Atlantic basin: simulations in nonlinear terrain-following coordinates. *Dyn. Atmos. Oceans* 32, 239–281.
- Haidvogel, D., Arango, H.G., Budgell, W., Cornuelle, B., Curchitser, E., Di Lorenzo, E., Fennel, K., Geyer, W., Hermann, A., Lanerolle, L., Levin, J., McWilliams, J., Miller, A., Moore, A., Powell, T., Shchepetkin, A., Sherwood, C., Signell, R., Warner, J., Wilkin, J., 2008. Ocean forecasting in terrain-following coordinates: formulation and skill assessment of the Regional Ocean Modeling System. *J. Comput. Phys.* 227, 3595–3624.
- Helly, J.J., Levin, L.A., 2004. Global distribution of naturally occurring marine hypoxia on continental margins. *Deep-Sea Res. Pt. I* 51, 1159–1168.
- Kalnay, E., Kanamitsu, M., Kistler, R., Collins, W., Deaven, D., Gandin, L., Iredell, M., Saha, S., White, G., Woollen, J., Zhu, Y., Leetmaa, A., Reynolds, R., Chelliah, M., Ebisuzaki, W., Higgins, W., Janowiak, J., Mo, K.C., Ropelewski, C., Wang, J., Jenne, R., Joseph, D., 1996. The NCEP/NCAR 40-year reanalysis project. *Bull. Am. Meteorol. Soc.* 77, 437–470.
- Kanamitsu, M., Kanamaru, H., 2007. 57-year California Reanalysis Downscaling at 10 km (CaRD10) part 1. *J. Climate* 20, 5527–5552.
- Köhö, A., Stammer, D., Cornuelle, B.D., 2007. Interannual to decadal changes in the ecco global synthesis. *J. Phys. Oceanogr.* 37, 313–337.
- Le Dimet, F., Talagrand, O., 1986. Variational algorithms for analysis and assimilation of meteorological observations: theoretical aspects. *Tellus A* 38(a), 97–110.
- Lewis, J.M., Derber, J.C., 1985. The use of adjoint equations to solve a variational adjustment problem with advective constraints. *Tellus A* 37, 309–322.

- Marchesiello, P., McWilliams, J.C., Shchepetkin, A., 2003. Equilibrium structure and dynamics of the California Current System. *J. Phys. Oceanogr.* 33, 753–783.
- McCreary, J.P., Kundu, P., Chao, S.Y., 1987. On the dynamics of the California Current System. *J. Mar. Res.* 45, 1–32.
- Moore, A.M., Arango, H.G., Di Lorenzo, E., Cornuelle, B.D., Miller, A.J., Neilson, D.J., 2004. A comprehensive ocean prediction and analysis system based on the tangent linear and adjoint of a regional ocean model. *Ocean Modell.* 7, 227–258.
- Nelson, C.S., 1977. Wind stress and wind stress curl over the California current. NOAA Tech. Rep. NMFS SSRF-714, Natl. Oceanic and Atmos. Admin., Silver Spring, MD.
- Pickett, M.H., Paduan, J.D., 2003. Ekman transport and pumping in the California Current based on the U.S. Navy's high-resolution atmospheric model (COAMPS). *J. Geophys. Res.* 108 (C10).
- Rykaczewski, R.R., Checkley, D.M., February 2008. Influence of ocean winds on the pelagic ecosystem in upwelling regions. *PNAS* 105 (6), 1965–1970.
- Seo, H., Miller, A.J., Roads, J.O., 2007. The Scripps Coupled Ocean-Atmosphere Regional (SCOAR) model, with applications in the eastern Pacific sector. *J. Climate* 20, 381–402.
- Shchepetkin, A.F., McWilliams, J.C., 2004. The Regional Oceanic Modeling System (ROMS): a split explicit, free-surface, topography-following-coordinate oceanic model. *Ocean Modell.* 9, 347–404.
- Smith, R.L., 1968. Upwelling. *Oceanogr. Mar. Biol. Ann. Rev.* 6, 11–46.
- Smith, T.M., Reynolds, R.W., 2004. Improved extended reconstruction of SST (1854–1997). *J. Climate*, 2466–2477.
- Snyder, M.A., Sloan, L.C., Diffenbaugh, N.S., Bell, J.L., 2003. Future climate change and upwelling in the California Current. *Geophys. Res. Lett.* 30 (15), 1823.
- Stammer, D., Wunsch, C., Giering, R., Eckert, C., Heimbach, P., Marotzke, J., Adcroft, A., Hill, C.N., Marshall, J., 2002. The global ocean circulation during 1992–1997, estimated from ocean observations and a general circulation model. *J. Geophys. Res.* (C9), 3118.
- Stewart, R.H., 2005. Introduction to Physical Oceanography. Texas A&M Univ, College Station, TX.
- Sverdrup, H.U., Johnson, M.W., Fleming, R.H., 1942. The Oceans: Their Physics, Chemistry, and General Biology. Prentice-Hall, Old Tappan, NJ.
- Thacker, W.C., 1989. The role of the hessian matrix in fitting models to measurements. *J. Geophys. Res.* 94 (C5), 6177–6196.
- Veneziani, M., Edwards, C.A., Doyle, J.D., Foley, D., 2009. A central California coastal ocean modeling study: 1. Forward model and the influence of realistic versus climatological forcing. *J. Geophys. Res.* 114, C04015.
- Winant, C.D., Dorman, C.E., 1997. Seasonal patterns of surface wind stress and heat flux over the Southern California Bight. *J. Geophys. Res.* 102, 5641–5653.